Volume 13
Number 41
7 November 2025
Pages 34973–35906

Journal of Materials Chemistry A

Materials for energy and sustainability

rsc.li/materials-a

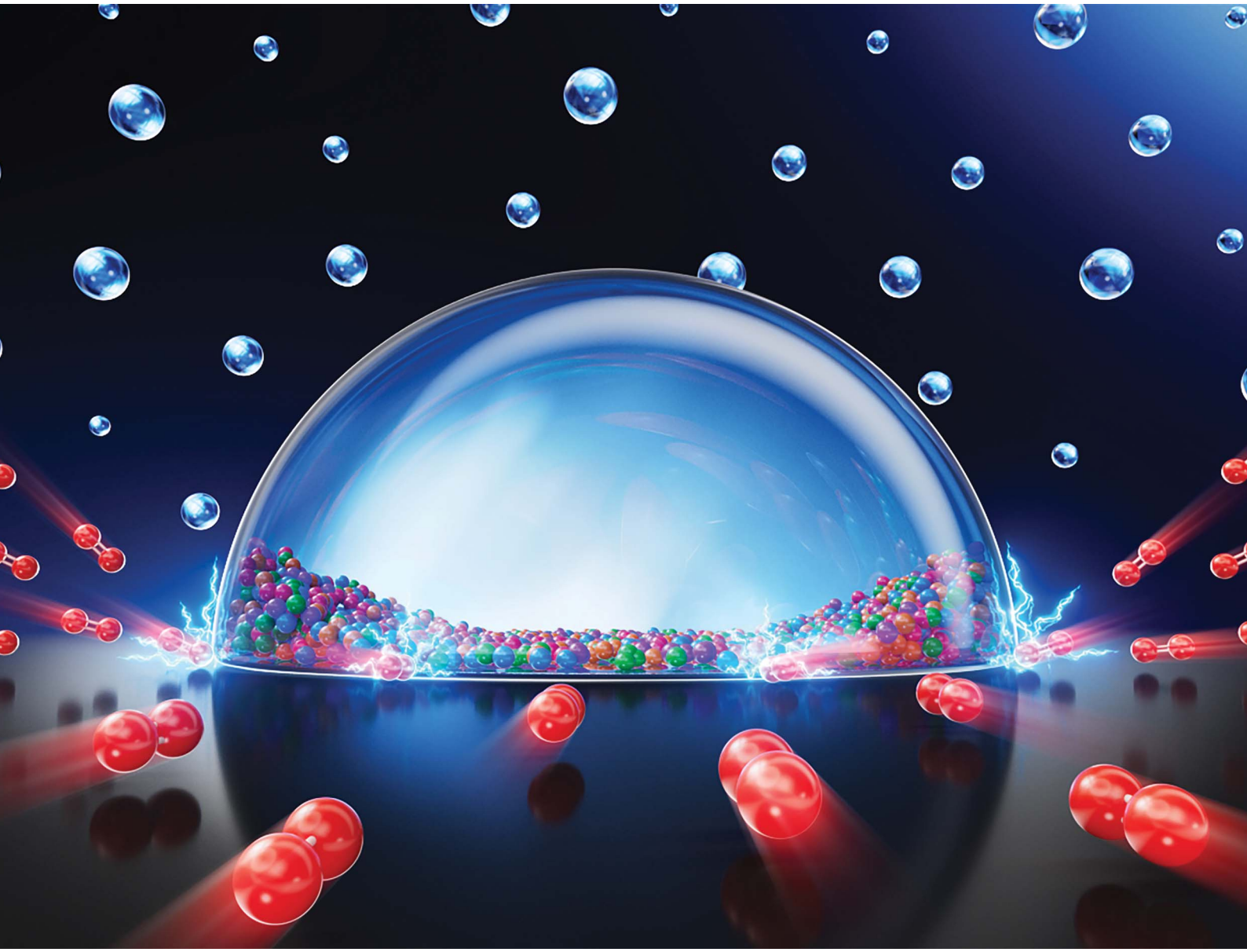

ISSN 2050-7488

ROYAL SOCIETY OF CHEMISTRY

PAPER

Jeffrey E. Dick *et al.*

Microdroplet-confined oxygen reduction forms highly active transition metal alloy hydroxides at low overpotentials for oxygen evolution

Journal of Materials Chemistry A

ROYAL SOCIETY OF CHEMISTRY

PAPER

View Article Online
View Journal | View Issue

Cite this: J. Mater. Chem. A, 2025, 13, 35220

Microdroplet-confined oxygen reduction forms highly active transition metal alloy hydroxides at low overpotentials for oxygen evolution

John F. Koons, [a] Samantha C. Cullom [a] and Jeffrey E. Dick *[ab]

The oxygen evolution reaction plays a key role in many modern energy conversion and storage devices, making the development of catalysts for the reaction of utmost importance. Transition metal hydroxides represent a promising category of oxygen evolution catalysts in alkaline environments, due to the affordability and abundance of material, high activity and good stability. However, precipitation of these catalysts directly on electrode surfaces can be energy intensive, requiring high overpotentials. In this work, we present a new method of electrodeposition using the confined environment of aqueous microdroplets adsorbed on an electrode to produce a high pH through heterogeneous reduction of solvated oxygen, O_2. Using O_2 reduction in this manner requires less cathodic applied potentials compared to other electrodeposition techniques and avoids direct metal reduction. Additionally, this methodology allows for the precipitation of a wide variety of stoichiometrically controlled transition metal hydroxides by only changing the starting metal precursor salts. Through this method, we precipitate a variety of transition metal hydroxides ranging from monometallic to penta-metallic alloys and analyze their morphology, composition and catalytic performance toward oxygen evolution. Overall, this work presents a new, facile method to be used toward electrodepositing a range of highly desirable transition metal hydroxide catalysts.

Received 9th July 2025
Accepted 13th August 2025

DOI: 10.1039/d5ta05555e

rsc.li/materials-a

Introduction

As the world moves toward a more renewable energy infrastructure, scientists have thoroughly investigated several chemical processes for converting and storing energy, with water electrolysis receiving much attention. Through water electrolysis, other sources of power such as solar, nuclear or wind can be used to produce hydrogen gas, H_2, which in turn can be converted to electrical energy *via* a variety of chemical processes.[1–4] Common electrolyzers today consist of an anode and cathode at which the oxygen evolution reaction (OER) and the hydrogen evolution reaction (HER), respectively, are driven by an applied potential. These reactions are ideally separated by 1.23 V, but due to kinetic limitations in both cases, devices never reach this ideal efficiency. OER especially suffers from sluggish kinetics due to its four-step, four-electron mechanism.[5] Some research has recently pursued catalysis of other anodic reactions such as chloride oxidation in seawater, urea electrolysis in wastewater, and glycerol oxidation to avoid OER's especially sluggish kinetics.[6–8] Still, the largest body of research in water electrolysis anodes remains focused on OER catalyst development.[1] IrO_2 catalysts perform exceptionally well in acidic solutions and RuO_2 performs on par or better in both acidic and alkaline solutions, but the cost and rarity of both metals limit their usefulness in industrializing water electrolysis.[9–13]

Transition metal-based catalysts offer a promising alternative to precious metal catalysts for OER. Recent years have seen the development of transition metal oxides, hydroxides, phosphides, and other similar materials with exceptional catalytic performance.[14–16] Currently, their usefulness in acidic water electrolysis devices like proton-exchange-membrane (PEM) electrolyzers is limited due to their instability at low pH.[17–19] However, transition metal oxides and hydroxides have exceptional stability in alkaline environments, making them promising candidates for catalysts in advanced alkaline water electrolyzers (AWEs), which account for most of the industrial level electrolyzers used today.[4,15,20,21] In recent years, researchers have made significant strides in finding a range of high-performance transition metal hydroxide compositions for OER catalysis and elucidating the catalytic mechanisms at work.[22–25] For example, Ni/Co-based hydroxides with small amounts of Fe either from coprecipitation or Fe impurities in water have been shown to have exceptionally low overpotentials, η, under alkaline conditions.[26–28]

Despite this progress in catalyst design and mechanistic understanding, the methods of synthesis remain relatively

[a]James Tarpo Jr. and Margeret Tarpo Department of Chemistry, Purdue University, West Lafayette, IN 47907, USA. E-mail: jdick@purdue.edu
[b]Elmore Family School of Electrical and Computer Engineering, Purdue University, West Lafayette, IN 47907, USA

underdeveloped. Many synthetic pathways utilize additives such as potassium hydroxide, hydrogen peroxide or bromine, often coupled with solvothermal methods to precipitate sheets of hydroxides on top of an electrode.[29–31] Still more methods utilize added base or nitrate/chloride anions to produce hydroxide at the electrode interface *via* water reduction, nitrate reduction, chloride oxidation, or some other mechanism to electro-precipitate catalysts directly on an electrode.[32–35] While these methods are relatively simple, there are some significant drawbacks. First, few universal methods exist across different transition metals or even different precursor salts (MCl_2, $M(NO_3)_2$, $M(SO_4)$, $M(ClO_4)_2$, *etc.*), which makes the development and optimization of methods for new stoichiometries and combinations labor intensive. Additionally, the reduction of water or nitrate anions require varying degrees of negative applied potentials at the working electrode for different metal combinations and concentrations. These potentials usually provide more than enough cathodic energy to electroreduce the metal itself to the zero-valent state rather than precipitating it as a hydroxide. Finally, while transition metal hydroxides are often synthesized as sheets, this geometry does not maximize electrocatalytic surface area (ECSA) per gram of material, and therefore, it may be useful for OER catalyst research to explore methods that allow for the precipitation of discrete nano- or micro-structures.

One seemingly unexplored methodology that could provide an answer to these considerations is that of electrodeposition *via* aqueous microdroplets suspended in a water-in-oil emulsion.[36,37] In this system, a small volume of aqueous solution (25 μL) containing relatively low concentrations of metal precursor salts is added to a larger volume of organic solvent (~5 mL) and sonicated to form an emulsion of aqueous microdroplets. Metal precursor salts are confined in these droplets due to insolubility in the organic phase, creating an electrochemical microreactor when the droplet collides with the electrode, irreversibly adsorbing to the surface. Electroneutrality is maintained in the droplet by partitioning of organic supporting electrolytes such as tetrabutylammonium perchlorate ($[TBA]^+[ClO_4]^-$) across the organic|aqueous phase boundary. This system has been used in the past to synthesize high entropy alloy nanoparticles and other materials by applying a cathodic potential in excess of −1.5 V *versus* 1 M Ag/AgCl to rapidly electrochemically reduce all metals in the droplet, along with water and any other species present.[38–40] However, a more subtle mechanism may be utilized at less cathodic applied potentials to quickly create a basic pH inside the droplet without reducing any metal. In addition to supporting electrolyte, the organic solvent will also dissolve significant amounts of gaseous oxygen, O_2, over time if exposed to ambient conditions. Therefore, if a cathodic potential is applied that is sufficiently negative to reduce O_2, a strongly basic pH gradient may be created inside the aqueous droplet. This will be aided by the subsequent partitioning of dissolved O_2 into the aqueous droplet from the O_2 rich organic phase in order to maintain concentration equilibrium across the two phases. Our group has recently shown that driving O_2 reduction during metal electrodeposition indeed creates such a basic environment in the droplet that it acts as a switch between depositing zero-valent Cu nanoparticles and $Cu(OH)_2$ nanoparticles.[41] Applying this now to a system where the aqueous microdroplets contain transition metals that reduce exclusively at more negative potentials than O_2 reduction (unlike Cu), it should be possible to achieve the selective precipitation of transition metal hydroxide catalysts by simply reducing dissolved O_2 in the aqueous phase.

Herein, we utilize this method of reducing O_2 in confined aqueous microdroplets to precipitate transition metal hydroxides. This method allows for the synthesis of a wide variety of compositions ranging from mono- to penta-metallic hydroxides with simple stoichiometric control by varying precursor salt concentrations. Importantly, this method avoids additives and only requires a small concentration and volume of metal precursor salt. It does not rely on electrochemical interactions with specific metal anions at the electrode interface and avoids the application of negative potential sufficient to electroreduce transition metals of interest, such as Ni, Co, Fe, Zn, and Mn. We investigate the structure, composition and catalytic performance of these materials, and gain mechanistic insights into the roles of O_2 reduction rate and droplet volume. This work introduces a facile new method to be used for the synthesis of a wide range of transition metal hydroxide nano- and microstructures without significant modification to the process while simultaneously avoiding unwanted electroreduction of metals during the process.

Experimental

Materials and instrumentation

Cobalt(II) chloride ($CoCl_2$) hexahydrate, manganese(II) chloride ($MnCl_2$) tetrahydrate, iron(III) chloride ($FeCl_3$) hexahydrate, nickel(II) chloride ($NiCl_2$) hexahydrate, zinc(II) chloride ($ZnCl_2$), tetrabutylammonium perchlorate $[TBA]^+[ClO_4]^-$, and 1,2-dichloroethane (>99.8%) (DCE) were purchased from Sigma Aldrich (St. Louis, MO). Potassium chloride (KCl) was purchased from Thermo Fisher Scientific (Waltham, MA). Ultrapure water (18.2 MΩ cm) was used for all aqueous solutions. 1.5 and 3 mm radius glassy carbon working electrodes, a 1 mm radius Pt working electrode, a platinum wire counter electrode, and 1 M KCl Ag/AgCl reference electrodes were purchased from CH Instruments (Austin, TX). All 1 M KCl Ag/AgCl electrodes were checked against an unadulterated 1 M KCl Ag/AgCl reference electrode against which all potential values were corrected and then converted to the reversible hydrogen electrode (RHE) throughout the manuscript. A carbon type B, 200 mesh Cu TEM grid from Ted Pella, Inc. (Redding, CA) was used as the working electrode when preparing samples for TEM. A fluorinated ethylene propylene Oak Ridge centrifuge tube was purchased from Thermo Fisher Scientific (Waltham, MA) and was used to prepare all emulsions. A horn sonicator from Sigma Aldrich (St. Louis, MO) was used to create emulsions. A CHI 6284E/F potentiostat from CH Instruments (Austin, TX) was used for all electrochemical measurements. An E3 Series GC rotating disk electrode and a Wave Vortex 10 electrode rotator from Pine Research Instrumentation (Durham, NC) were used for rotating disk experiments for catalyst stability.

Preparation of emulsion and electroprecipitation of catalyst

Solutions of 100 mM transition metal chloride salts in ultrapure water and 100 mM $[TBA]^+[ClO_4]^-$ in 1,2-dichloroethane were prepared. 5 mL of the 1,2-dichloroethane solution was added to a fluorinated centrifuge tube followed by 25 μL of the aqueous solution. This mixture was emulsified using a horn sonicator operating at 20 kHz for 30 s with 5 s sonication and 5 s rest cycles. The emulsion was poured into an electrochemical cell with a glassy carbon, TEM grid, or Pt working electrode, Pt wire counter electrode and a 1 M KCl Ag/AgCl reference electrode. The reference electrode was contained in a 1 M KCl solution and electrically connected with an agarose salt bridge. Prior to electrodeposition, the working electrodes (except for TEM grids) were polished first with 1 and 0.3 μm Type DX gamma alumina powder (Electron Microcopy Sciences) on a microcloth polishing pad (BASi Research Projects) and then polished again on a clean microcloth pad to remove excess alumina. The working electrodes were dipped in the emulsion with the salt bridge and counter electrode prior to applying a potential to allow the aqueous microdroplets to irreversibly adsorb to the working electrode surface. When electrodepositing from a bulk aqueous solution the electrodes were submerged directly in the aqueous solution. When electrodepositing from a 1 μL droplet, the droplet was pipetted directly on the electrode, and the electrode was flipped upside down and submerged in a 1,2-dichloroethane solution. A cathodic potential was applied to the working electrode for the specified times listed in the main text using a CHI6284E/F potentiostat. The emulsion is typically stable for at least 20 minutes, allowing ample time for electrodeposition. Following the experiment, working electrodes were submerged in acetone for 5 minutes, ultrapure water for 5 minutes, and ethanol for 1 minute. Electrodes were air dried before characterization.

When preparing samples for TEM characterization, the working electrode was a TEM grid electrically connected by tweezers to the potentiostat. The same washing procedure was used for TEM grids; however, they were stored in vacuum for 1 hour to remove excess solvent before characterization.

Electron microscopy and X-ray characterization

SEM characterization utilized an Apreo 2S, a Quanta 650 FEG, and a Teneo Volumescope (FEI, Hillsboro, OR). EDX was done using an Oxford Aztec Xstream-2 silicon drift detector with Xmax 80 mm window (Oxford Instruments, High Wycombe, UK). TEM characterization was done using a Talos 200i with high-angle annular darkfield and EDX detectors from Thermo Fisher Scientific (Waltham, MA). XPS spectra were collected using a Kratos AXIS instrument (Kratos Analytical, Nanuet, NY). An aluminum K-edge source was used with a pass energy of 20, a work function of −4.36, and an energy step of 0.050 eV. XPS peaks were fit using CasaXPS software.

Electrocatalysis

Transition metal hydroxides were precipitated on a glassy carbon working electrode and washed using the method above. Following the electroprecipitation and washing steps, the open circuit potential (OCP) of the precipitate coated, or clean glassy carbon working electrode was determined using the potentiostat and a 1 M KCl Ag/AgCl reference electrode in a solution of 0.1 M KOH. Following this, we ran linear sweep voltammograms in a potential window ± 50 mV from the OCP (*i.e.* 0.1 V to 0 V if OCP is 0.05 V) at a range of scan rates (5, 10, 25, 50, 100, 250, 500; all in mV s^{-1}) with a quiet time of 10 s. Linear sweep voltammograms were run in both scan directions. The resulting capacitive current was plotted *versus* scan rate, with the slope giving the double layer capacitance. This value was then divided by a specific capacitance value of 0.04 mF cm^{-2} to give the electrocatalytic surface area. See SI for these plots. For conversion of potentials from 1 M KCl Ag/AgCl to the RHE, we measured a pH of 12.88 ± 0.01 for the 0.1 M KOH solution. The uncompensated resistance, R_u, of this solution was measured to be 29.34 Ω. Both pH and R_u were determined using a Thermo Fisher Orion Versa Star Pro with a ROSS Sure-Flow pH electrode and a 013005MD 4-cell conductivity probe, respectively. Conductivity measurements were converted from Siemens per cm to Ohms by dividing by a cell constant of 0.475 cm and taking the reciprocal. Stability tests of the catalysts were carried out with a rotating disk electrode (RDE) rotating at 1600 rpm. An anodic current of 1 mA (calculated to be 10 mA cm^{-2}) was applied for 7200 s. Linear sweep voltammograms were taken before and after the stability tests to show changes in catalytic activity.

Results and discussion

To test whether transition metal hydroxides can be precipitated by driving O_2 reduction in aqueous microdroplets, we first

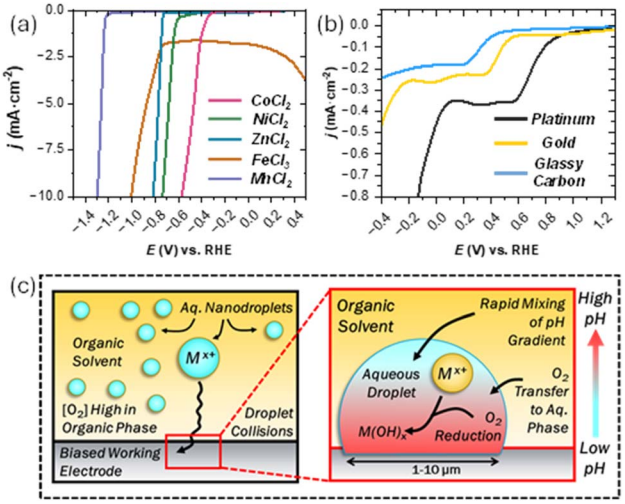

Fig. 1 (a) Linear sweep voltammograms of 50 mM solutions of $CoCl_2$, $NiCl_2$, $ZnCl_2$, $FeCl_3$, and $MnCl_2$ added into the aqueous microdroplets suspended in an emulsion on a glassy carbon working electrode. (b) Linear sweep voltammograms of O_2 reduction on platinum, gold and glassy carbon working electrodes in 1 M KCl. (c) Schematic showing a broad view of aqueous microdroplets colliding with the working electrode, and a zoomed view illustrating the pH gradient and precipitation process produced by reducing O_2 in the aqueous droplets.

determined the reduction potentials of the metal salts on a glassy carbon electrode (Fig. 1a). We chose five metals (Mn, Fe, Co, Ni, and Zn) with reduction potentials between −0.25 and −1.3 V *vs.* RHE. These reduction onset potentials are all significantly more cathodic than that of O_2 reduction, which has onset potentials between approximately 1 V and 0.4 V *vs.* RHE depending on the electrode material (Fig. 1b). This relationship allows us to selectively reduce O_2 and not any of the metal salts at potentials less cathodic than approximately −0.25 V *vs.* RHE. Importantly, the reduction peak seen for iron(III) chloride ($FeCl_3$) at more positive potential corresponds to the reduction of Fe(III) to Fe(II), which does not result in any electrodeposition.

The method for electrodepositing transition metal hydroxides by selectively reducing O_2 in aqueous microdroplets is illustrated in Fig. 1c. Metal chloride salts are confined inside of aqueous microdroplets that are suspended in a continuous phase of 1,2-dichloroethane which contains $[TBA]^+[ClO_4]^-$ as an electrolyte. These aqueous droplets will collide randomly with the working electrode as they diffuse throughout the emulsion. After this, they become electrically connected to the working electrode and serve as nano- or picoliter volume reactors. When the working electrode is held at a sufficiently cathodic potential to drive O_2 reduction in the droplets and not reduce any of the metal cations directly – between 0.4 V and −0.25 V *vs.* RHE for a glassy carbon working electrode – a basic pH gradient will be created in the droplet by O_2 reduction either consuming protons in acidic conditions or producing hydroxide in basic conditions as seen in eqn (1)–(4),[42] Once dissolved O_2 in the aqueous droplet is reduced more O_2 should continually partition into the aqueous droplet from the higher concentration dissolved in the surrounding organic phase to maintain an equilibrium concentration gradient. Hence there will be a constantly replenishing source of O_2 to be reduced in the aqueous droplets, causing a sharp increase in pH.

Acidic conditions:

$$O_2 + 4H^+ + 4e^- \rightleftharpoons 2H_2O \quad (1)$$

$$O_2 + 2H^+ + 2e^- \rightleftharpoons H_2O_2 \quad (2)$$

Basic conditions:

$$O_2 + 2H_2O + 4e^- \rightleftharpoons 4OH^- \quad (3)$$

$$O_2 + H_2O + 2e^- \rightleftharpoons HO_2^- + OH^- \quad (4)$$

Applying the results of the cyclic voltammograms in Fig. 1, we used an applied cathodic potential, $E_{appl,}$ of −0.2 V *vs.* RHE for 400 s to a glassy carbon working electrode that was submerged in a water-in-oil emulsion as seen in Fig. 1c, readily reducing aqueous dissolved O_2, while not reducing any of the metal salts. In this first case, the aqueous droplets contained $CoCl_2$, $NiCl_2$, $ZnCl_2$, $FeCl_3$, and $MnCl_2$. The resulting current–time (*i*–*t*) curve is seen in Fig. S1, showing a large current for its entirety as would be expected from O_2 reduction at that E_{appl}. The SEM image in Fig. 2a shows some of the common resulting morphologies of the precipitated material on the electrode surface. They range from sheets in the μm range to single particles in the nm range and appear to be randomly distributed across the surface (Fig. S2). In many cases, the precipitated material resides primarily in a ring-like structure likely along the edge of the collided droplet where the water|oil|electrode interface was located (Fig. S3). The abundance of cases with most material focused on the edge of the droplet collision suggests that the interface is the source of the high pH gradient due to O_2 partitioning in and being subsequently reduced. However, the rings do not appear in every case, highlighting the stochastic and heterogeneous nature of these droplet collisions.

Fig. 2b(i) shows a STEM-HAADF image of the $MnFeCoNiZn(OH)_x$ sheet precipitated on a carbon TEM grid. The image displays a heterogeneous distribution of the transition metals across the sheet, seen as the high scattering bright areas. This heterogeneity was consistent for nearly all cases (Fig. S4). A higher magnification HAADF image in Fig. 2b(ii) reveals rows of atoms with a *d*-spacing of 0.250 nm. While, this value alone cannot be directly correlated with any specific transition metal layered double hydroxide (LDH), it does highlight the crystalline nature of the transition metal rich regions. Other areas of the transition metal-rich regions of the precipitate revealed similar crystalline nature (Fig. S5). In contrast, regions of the precipitate with a less abundant metal signal revealed no obvious signs of crystalline fringes in HAADF (Fig. S6). Overall, this reveals a mix of crystalline and amorphous regions in the transition metal precipitates. X-ray diffraction (XRD) could provide further insight into the crystal planes present in these precipitates, but this characterization method has proven to be very limited at characterizing metals deposited from nano- or microdroplets, likely due to relatively low surface coverage and the randomness of precipitate orientation.

Fig. 2c shows EDX mapping of an SEM image for Mn, Fe, Co, Ni, and Zn – all of which were originally contained in the aqueous droplets. All 5 metals were present in the precipitates and consistently appeared to have a homogeneous distribution. Significantly, chlorine and nitrogen signals were largely absent from these materials, which would be present if the precipitates were either metal chloride salts or some complex with the organic $[TBA]^+$ salt, respectively (Fig. S7). Instead, the lack of signal suggests precipitation of transition metal hydroxides rather than salt complexes. Fig. 2d shows the EDX ratios of each metal and their standard deviations. These results indicate that the transition metal precipitates are at the high end of mid-entropy with a $\Delta S_{conf} = 1.56R \pm 0.028$ (Fig. S8). STEM/EDX also revealed a homogeneous and random distribution of metals across the precipitates (Fig. S9). The homogenous distribution of all five transition metals suggests that the microdroplet confined O_2 reduction method is generalizable for multiple transition metals as expected.

While the E_{appl} value and EDX data indicate that the metals are likely precipitated as transition metal hydroxides, XPS provides clearer insight into the specific transition metal and oxygen species present. For XPS characterization, we coprecipitated Mn, Fe, Co, Ni, and Zn for 1200 s (*versus* the original 400 s) at the same E_{appl} on a glassy carbon working electrode. This increase in reaction time allows for more randomly diffusing

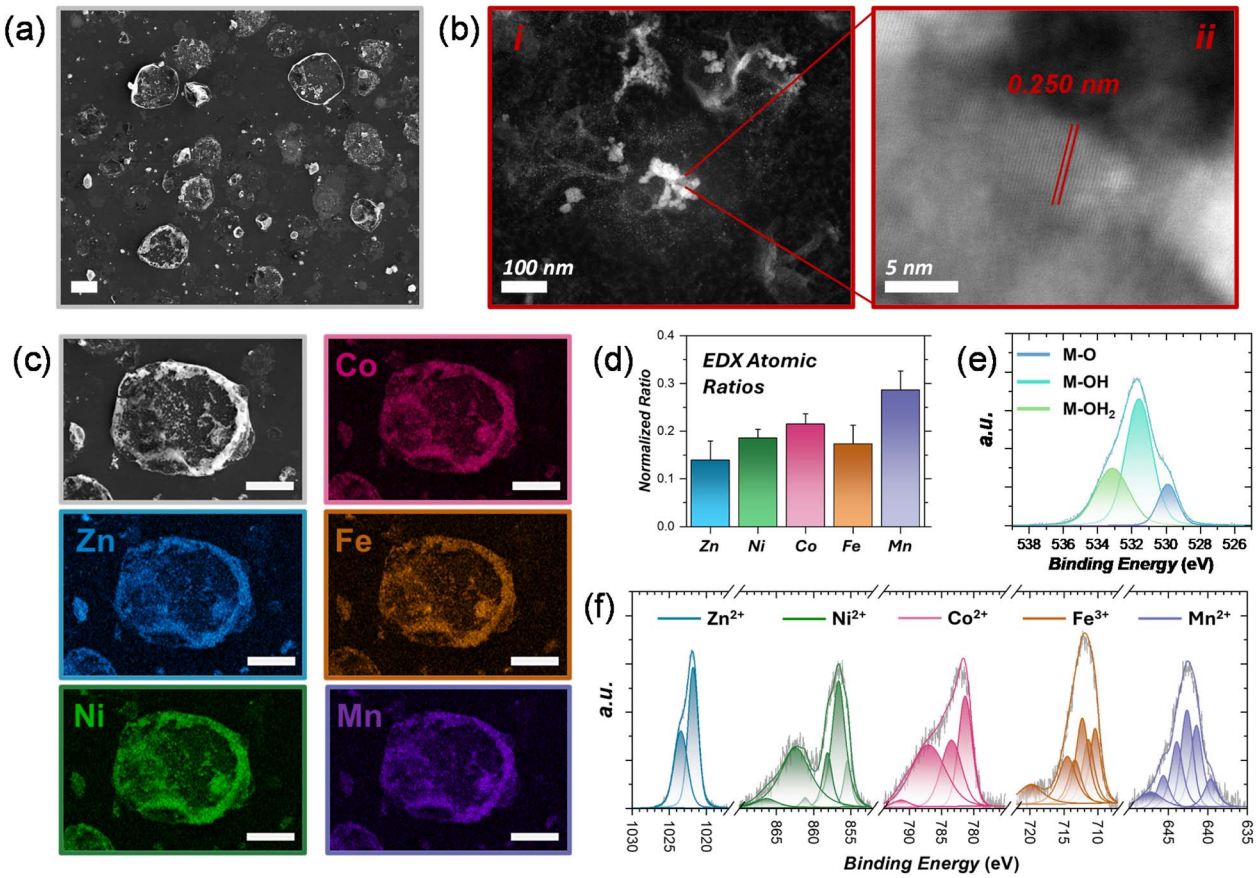

Fig. 2 (a) SEM image of metals precipitated at −0.2 V *vs.* RHE showing diversity of morphologies. (b) STEM-HAADF image of large precipitate at (i) low zoom and (ii) high zoom with *d*-spacing specified for crystalline fringes. (c) SEM image and corresponding EDX mapping of different metals in electroprecipitated materials (scale bars are 10 μm unless otherwise specified). (d) Ratios of constituent metals in precipitated materials (error bars are standard deviation). (e) XPS O_{1s} peak and (f) transition metal 2p peaks.

droplets in the emulsion to collide with the cathodically biased working electrode and increases the surface coverage of catalyst. The full XPS survey spectrum obtained for the sample can be seen in Fig. S10. In Fig. 2e the O_{1s} signal indicates a majority peak that corresponds well with typical transition metal hydroxide (M–OH) binding energies, with a smaller peak consistent with transition metal oxide (M–O) binding energies. The water peak (M–OH_2) aligns well with values assigned to surface oxidation layers formed on certain transition metal hydroxides resulting from moisture in the air.[31,43,44] Fig. 2f shows the different 2p regions for Mn, Fe, Co, Ni, and Zn. The regions showed no indication of zerovalent or monovalent signals. Rather, all peaks fit exclusively for either hydroxide or (oxy)hydroxide species of each metal.[43] In all cases, the metals are still present in the original valency of the metal chloride salt, indicating a lack of metal electroreduction at the electrode surface. Together these XPS data demonstrate that the MnFeCoNiZn hydroxides are being precipitated *via* hydroxide or oxide formation with no competing electroreduction of the metals themselves, thereby maximizing the amount of metal precursor salt that forms the desired catalytic product rather than zerovalent metal structures.

In addition to precipitating all five metals together, we also precipitated them separately by adding 25 mM of each metal salt into the aqueous phase. We observed similar morphologies for the individual cases compared with the penta-metallic hydroxide (Fig. S11). This again highlights the generalizability of this technique in its ability to precipitate transition metals both individually and as alloys.

Having precipitated five transition metals together in a homogeneous and nearly equimolar ratio, we sought to explore the level of control over the relative amounts of each metal in a case with just two starting components. We tested Ni and Fe together since hydroxide alloys of these materials have been shown to have superior catalytic performance toward OER.[25,28,45] Specifically, alloys with a ratio of $Ni_{0.75}Fe_{0.25}$ perform exceptionally well in basic environments. We added 75 mM $NiCl_2$ and 25 mM $FeCl_3$ to the aqueous phase in the water-in-oil emulsion and used the same E_{appl}, −0.2 V *vs.* RHE, on a glassy carbon working electrode for 400 s. The resulting precipitates, seen in Fig. 3a, had similar morphologies to the previous cases. EDX mapping of the $NiFe(OH)_x$ precipitates shows a mostly homogeneous distribution of both metals (Fig. 3b and c). EDX point scans of the bimetallic precipitates revealed a range of atomic ratios centered around the target value of a 75 : 25 Ni : Fe

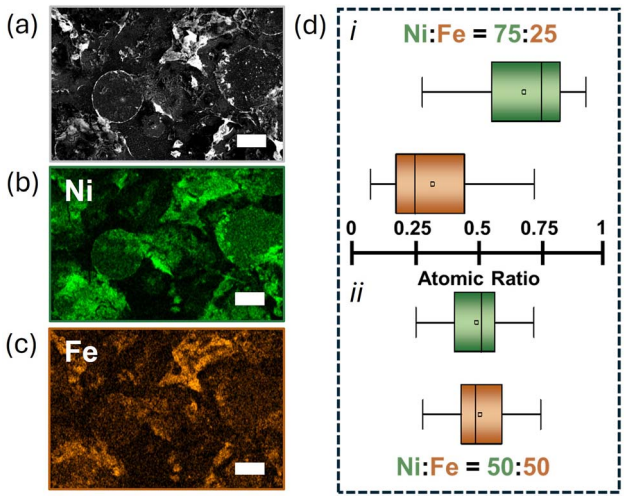

Fig. 3 (a) SEM image of precipitates resulting from adding 75 mM $NiCl_2$ and 25 mM $FeCl_3$ in the aqueous phase before emulsifying and precipitating on a glassy carbon electrode at −0.2 V *vs.* RHE. (b) Ni and (c) Fe EDX maps of the precipitates shown in (a). (d) Resulting atomic ratios determined by EDX of Ni and Fe when either a (i) 75 : 25 or (ii) 50 : 50 atomic ratio of Ni : Fe metal precursor salts were originally added to the aqueous phase.

atomic ratio (Fig. 3d(i)). While the mean and median values are approximately equal to the ratios of each metal added to the aqueous phase, there is a significant amount of deviation around those values. We also demonstrated this with a 50 : 50 Ni : Fe ratio added to the aqueous phase, which yielded the atomic ratios seen in Fig. 3d(ii). Once again, the mean and median are centered near the target value with some deviation. While some heterogeneity occurs in the precipitation of $NiFe(OH)_x$, O_2 reduction in aqueous microdroplets shows significant promise in its ability to selectively precipitate specific ratios of these starting metals by simply adding the desired ratio of the metal precursor salts without having to change anything else about the procedure.

We next sought to gain more insight into the mechanism of microdroplet mediated precipitation *via* O_2 reduction by comparing our results to those attained by applying the same potential to an electrode either suspended in a bulk aqueous phase with no adsorbed droplets or suspended in an organic phase with a large adsorbed aqueous droplet (approximately 1 mm radius and 1 μL volume). Given that pH is a function of H^+ concentration, its value will not only depend on the physical number of H^+ molecules in a droplet, but also the volume of the droplet. Imagining shrinking the radius of a droplet from the scale of 1 mm down to 1 μm, both the size of the water|oil|electrode interface and the volume of the droplet will change significantly. Decreasing the radius will decrease the droplet contact interface with the electrode in proportion to the radius since the circumference is equal to $2\pi r$. Hence the amount of O_2 reduced may also experience a decrease that is roughly proportional to the droplet radius. However, volume is equal to $\frac{4}{3}\pi r^3$ meaning that volume will have a much sharper decrease compared to the size of the water|oil|electrode interface as the droplet radius shrinks. Applying this to the formula for concentration, $\frac{n}{V}$, where n is moles and V is volume, we can see that shrinking a droplet will result in larger changes in concentration of species such as H^+ and OH^-. Consequently, aqueous microdroplets likely provide a much more suitable environment for precipitating transition metal hydroxides compared to larger droplets, which might not sufficiently concentrate the produced OH^-. Additionally, not only will a bulk aqueous environment fail to confine any OH^-, but it also likely contains too low of a concentration of dissolved O_2 to precipitate the catalysts.

To investigate this theory, we applied 0.47 V, 0.22 V and −0.03 V *vs.* RHE to these three different environments – a bulk aqueous phase, a 1 μL aqueous droplet and an emulsion of aqueous microdroplets. Fig. 5a shows where each of these potentials fall on the reduction curve of O_2 reduction in 0.1 M KCl, and are marked by E_{appl} 1, 2, and 3, respectively. In the case of a bulk aqueous phase containing 20 mM each of $MnCl_2$, $FeCl_3$, $CoCl_2$, $NiCl_2$, and $ZnCl_2$, we saw no precipitation or electrodeposition of the metals at any of these potentials (Fig. S12) – likely due to the insufficient O_2 concentration and diffusion of any basic pH gradient formed away from the electrode surface that it was formed at. In the case of a 1 μL droplet adsorbed on the electrode, there was a small amount of precipitation around the interface only at −0.03 V (Fig. S13), which is consistent with previous observations and may be due to a localized pH gradient at the interface.[46] The preferential formation of precipitate around the interface likely indicates once again that the O_2 reduces primarily around the interface as soon as it partitions into the aqueous droplet. This effect is more pronounced in large droplets since OH^- will only be concentrated at this point before diffusing away into the larger aqueous volume of the droplet. Our group is currently investigating ways to visualize this interfacial pH effect and its potential ability to form precipitate rings further.

We next applied all three of these potentials to a glassy carbon working electrode submerged in an emulsion of aqueous microdroplets for 120 s. The resulting current densities, j, on the j–t curves for E_{appl} 1, 2 and 3 were about 0.01 mA cm^{-2}, 0.04 mA cm^{-2} and 0.2 mA cm^{-2}, respectively (Fig. 4b), which reflect the j of O_2 reduction driven at each E_{appl}. Additionally, we held a fourth electrode at the open circuit potential (OCP) for 120 s, during which no bias or current is applied as the potential is held at the OCP, which was about 1.1 V *vs.* RHE (Fig. S14). In all four of these cases, transition metal precipitates were formed with a range of compositions.

Fig. 4c–f show SEM images of the precipitated materials in each case and the EDX ratios of these precipitates. Fig. 4c shows the precipitates formed when holding the electrode at the OCP and passing negligible current. We found it surprising that precipitation happened in this case, and that the materials showed no chloride peak in EDX (Fig. S15). These materials were hydroxide alloys of Ni and Fe in a ratio of approximately $Fe_{0.85}Ni_{0.15}$. This precipitation likely occurs through some spontaneous galvanic interaction with another species in the

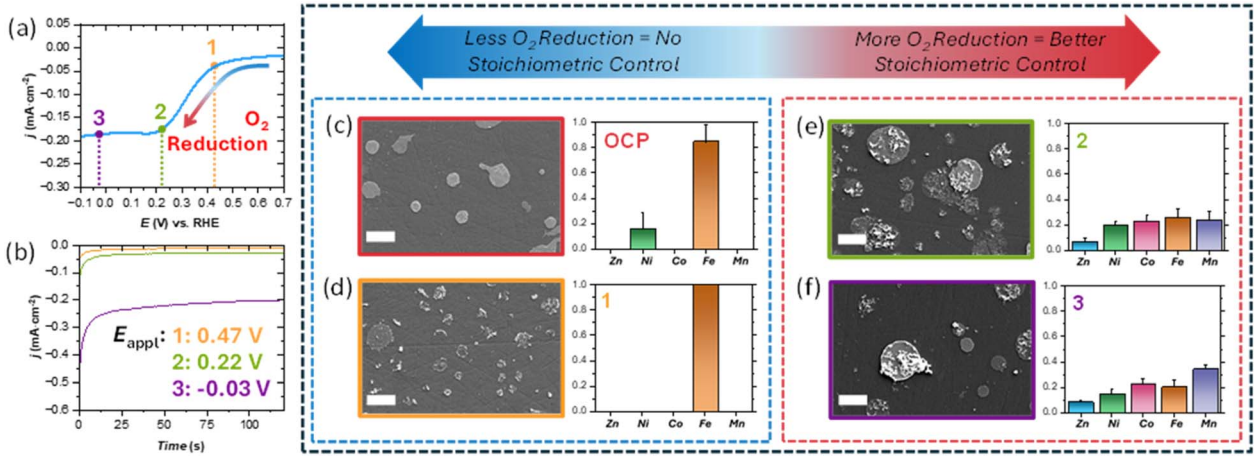

Fig. 4 (a) Linear sweep voltammogram showing three different E_{appl} values and where they lie on the O_2 reduction curve. (b) Corresponding j–t curves after applying each E_{appl} for 120 s. SEM image and EDX atomic ratios at (c) OCP, (d) E_{appl} 1, (e) E_{appl} 2 and (f) E_{appl} 3.

aqueous droplets but the exact cause remains unclear. Fig. 4d shows precipitates synthesized at E_{appl} 1, which have more similar morphologies to those precipitated at −0.2 V *vs.* RHE compared to the films formed at OCP, but EDX analysis of these revealed that the materials only contained Fe. The precipitates formed at E_{appl} 2 in Fig. 4e and at E_{appl} 3 in Fig. 4f displayed the most similar morphologies and atomic ratios of all 5 metals compared to those deposited at −0.2 V. These observations show that increased levels of O_2 reduction lead to better stoichiometric control over the resulting transition metal hydroxides.

The variety of precipitate morphologies and compositions might be explained by Pourbaix diagrams and the relative pH sensitivity of each metal. All of the metals used in these cases – Mn, Fe, Co, Ni, Zn – are likely to form hydroxides, oxides or oxyhydroxides rather than be reduced by the electrode at all three values of E_{appl}, given that a sufficiently basic pH is present in the droplet.[47,48] Mn requires the most basic pH to form precipitates, suggesting that a pH value of 10 or higher is present when Mn is precipitated. However, the pH in the microdroplets likely does not reach this value when the electrode is held at E_{appl} 1 or OCP. Despite this, Fe will precipitate as an (oxy)hydroxide even at low pH values, possibly explaining why it is still present in all four cases. Still, the mechanism of precipitation at OCP and the reason for Ni coprecipitating with Fe are not yet fully clear – especially given that these materials are produced without passing any current. Given that many intriguing spontaneous redox phenomena have been observed at the water|air and water|oil interfaces in aqueous microdroplets, it will be an interesting avenue of inquiry to probe this mechanism further.[49–54] This drastic change in pH based on slight changes in E_{appl} is enabled both by the confinement of the aqueous microdroplets and the continuous O_2 supply from the surrounding organic phase. Consequently, this method is likely compatible with any organic solvent that has a higher O_2 solubility than water and will create a stable emulsion with water. Solvents such as chloroform and dichloromethane have been shown to work similarly to 1,2-dichloroethane in multiphase electrochemistry applications, and we expect that they will also work well for this method.

Finally, we tested the utility of $MnFeCoNiZn(OH)_x$, $Ni(OH)_2$, and $Ni_{0.75}Fe_{0.25}(OH)_x$ as OER catalysts in 0.1 M KOH (Fig. 5a). These materials were precipitated onto glassy carbon electrodes using the same method as above. $Ni(OH)_2$ was synthesized by adding 100 mM $NiCl_2$ to the aqueous phase. The electrocatalytic surface area (ECSA) of each of these materials was estimated by determining the double layer capacitance, C_{dl}, and dividing by the specific capacitance of the materials.[34] C_{dl} was estimated by plotting the capacitive current *versus* potential scan rate while doing linear sweep voltammetry in a purely capacitive potential window (Fig. S16–S19). Details for these calculations can be seen in the Experimental Section and SI. We found that the $MnFeCoNiZn(OH)_x$ had an onset potential – set as the potential at which $j = 10$ mA cm^{-2} – of approximately 1.8 V *vs.* RHE. $Ni(OH)_2$ yielded a nearly identical onset potential. $Ni_{0.75}Fe_{0.25}(OH)_x$ had an onset potential of approximately 1.75 V *vs.* RHE. All three had a far lower onset potential than the undecorated glassy carbon macro electrode, which was about 2.6 V *vs.* RHE. These onset potential values represent OER overpotentials, η, of 0.57 V for $MnFeCoNiZn(OH)_x$ and $Ni(OH)_2$, and 0.52 V for $Ni_{0.75}Fe_{0.25}(OH)_x$. While these η values are over 100 mV larger than the lowest reported catalysts, they nevertheless show that this technique can be used to electrodeposit active catalytic materials toward OER. We also tested the precipitates formed in Fig. 4, all of which exhibited similar η values (Fig. S20–S24).

In addition to determining the η of these catalysts, we also tested their stability when doing OER in 0.1 M KOH. Fig. 5b shows chronopotentiograms where the catalysts were held at $j =$ 10 mA cm^{-2}. All three showed relatively stable behavior with slight increases in η over the course of 2 hours. The slight discrepancies in η values between the original linear sweep voltammograms likely results from different coverages of precipitate between different electroprecipitation trials. The droplets' rate of collision with the electrode will differ in subsequent trials due to the stochastic nature, which will cause slight variations in catalyst ECSA. Linear sweep voltammograms

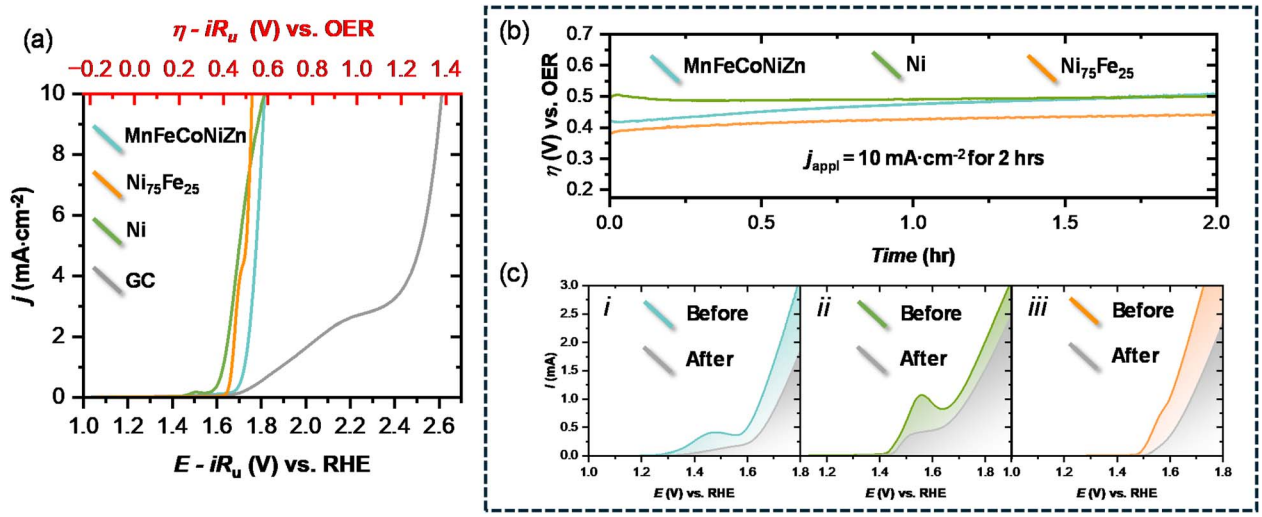

Fig. 5 (a) Linear sweep voltammograms of a glassy carbon electrode with $MnFeCoNiZn(OH)_x$, $Ni_{75}Fe_{25}(OH)_x$, $Ni(OH)_2$ or no catalyst (GC) electrodeposited on the surface in 0.1 M KOH. (b) Galvanostatic stability tests of the three catalysts on a rotating disk electrode (RDE) at 1600 rpm and $j = 10$ mA cm^{-2} for 2 hours. (c) Linear sweep voltammograms of (i) $MnFeCoNiZn(OH)_x$, (ii) $Ni(OH)_2$ and (iii) $Ni_{75}Fe_{25}(OH)_x$ before and after the two-hour stability tests on the RDE.

from before and after the 2 hour testing time also show a slight decrease in catalytic performance over time, as seen by the decreased i following stability testing (Fig. 5c(i)–(iii)). To determine the cause of this catalytic loss, we ran the $MnFeCoNiZn(OH)_x$ catalyst until it changed to the η expected for glassy carbon (Fig. S26). After imaging this electrode, it was determined that the catalyst had fallen off of the surface and only ClO^- salt remained – possibly due to oxidation of Cl^- impurities in solution (Fig. S27). Finally, a linear sweep voltammogram confirmed that the electrode only showed the electrochemical characteristics of a glassy carbon electrode. Overall, the catalyst precipitates themselves appear to be relatively stable, but the glassy carbon substrate is not ideal for long term catalysis. Despite this issue on glassy carbon, it remains an interesting avenue of inquiry to test this technique on other materials commonly used for OER catalyst substrates such as a Ni foam or C mesh. Since this method relies on reducing dissolved aqueous O_2, it should be viable on other electrode materials as long as they reduce O_2 at less cathodic potentials than the added aqueous metal salts, which we demonstrated on a Pt working electrode (Fig. S28).

Conclusion

In this work we use aqueous microdroplets suspended in a water-in-oil emulsion as isolated microreactors to drive strong pH gradients and precipitate transition metal hydroxides directly on an electrode. We precipitate a penta-metallic alloy of $MnFeCoNiZn(OH)_x$, monometallic hydroxides, and bimetallic hydroxides, investigating their structure, stoichiometric control and catalytic activity. Additionally, we investigate the mechanism of precipitation to show the importance of microdroplets and reduction of dissolved O_2. This method takes advantage of the high O_2 solubility in organic solvents to provide a constantly replenishing supply of O_2 to be reduced inside of the aqueous microdroplets. The produced OH^- ions are confined in the aqueous phase, creating a high pH that precipitates transition metal ions as hydroxides. By using O_2 reduction to create a basic environment, this method requires less cathodic potentials than water or NO_3^- reduction, thus avoiding any unwanted direct reduction of the metals. Additionally, this pH gradient allows for generalizable precipitation of multiple different transition metals separately or together, along with simple stoichiometric control of the synthesized catalysts. Overall, this method opens a new synthetic approach to producing transition metal hydroxides *via* pH gradients in aqueous microdroplets and opens avenues for scientists to use confined microreactors to synthesize materials in new and interesting ways directly on an electrode.

Author contributions

J. F. K. and S. C. C. performed all experiments and electron microscopy characterization. J. F. K. carried out electrocatalysis and XPS characterization. J. F. K., S. C. C., and J. E. D. all contributed to the development and writing of the manuscript. J. E. D. supervised all aspects of the research. All authors have reviewed and approved the final version.

Conflicts of interest

The authors have no conflicts of interest to declare.

Data availability

All raw data has been made available in the excel sheets submitted as part of the SI. See DOI: **https://doi.org/10.1039/d5ta05555e**.

Acknowledgements

The authors would like to acknowledge the use of facilities within the Purdue Electron Microscopy Center. Facility RRID SCR_022687. XPS data were obtained at the Surface Analysis Facility of the Birck Nanotechnology Center at Purdue University. The research was sponsored by the Army Research Office and was accomplished under grant number W911NF-24-1-0199. The views and conclusions contained in this document are those of the authors and should not be interpreted as representing the official policies, either expressed or implied, of the Army Research Office or the U.S. Government. The U.S. Government is authorized to reproduce and distribute reprints for Government purposes notwithstanding any copyright notation herein.

References

1 L. Peng and Z. Wei, *Engineering*, 2020, **6**, 653–679.
2 C. Lamy, *Int. J. Hydrogen Energy*, 2016, **41**, 15415–15425.
3 M. El-Shafie, *Results Eng.*, 2023, **20**, 101426.
4 A. Ursua, L. M. Gandia and P. Sanchis, *Proc. IEEE*, 2011, **100**, 410–426.
5 T. Schuler, T. Kimura, T. J. Schmidt and F. N. Büchi, *Energy Environ. Sci.*, 2020, **13**, 2153–2166.
6 Y. Feng, X. He, M. Cheng, Y. Zhu, W. Wang, Y. Zhang, H. Zhang and G. Zhang, *Small*, 2023, **19**, 2301986.
7 H. Xie, Y. Feng, X. He, Y. Zhu, Z. Li, H. Liu, S. Zeng, Q. Qian and G. Zhang, *Small*, 2023, **19**, 2207425.
8 J. Fan, X. Xiang, Y. Liu, X. Yang, N. Shi, D. Xu, C. Zhou, M. Han, J. Bao and W. Huang, *SusMat*, 2025, e70010.
9 S. Cherevko, S. Geiger, O. Kasian, N. Kulyk, J.-P. Grote, A. Savan, B. R. Shrestha, S. Merzlikin, B. Breitbach, A. Ludwig and K. J. J. Mayrhofer, *Catal. Today*, 2016, **262**, 170–180.
10 Y. Li, W. Wang, M. Cheng, Y. Feng, X. Han, Q. Qian, Y. Zhu and G. Zhang, *Adv. Mater.*, 2023, **35**, 2206351.
11 T. Reier, M. Oezaslan and P. Strasser, *ACS Catal.*, 2012, **2**, 1765–1772.
12 W. H. Lee, Y.-J. Ko, J. H. Kim, C. H. Choi, K. H. Chae, H. Kim, Y. J. Hwang, B. K. Min, P. Strasser and H.-S. Oh, *Nat. Commun.*, 2021, **12**, 4271.
13 Y. Lee, J. Suntivich, K. J. May, E. E. Perry and Y. Shao-Horn, *J. Phys. Chem. Lett.*, 2012, **3**, 399–404.
14 S. Kumaravel, K. Karthick, S. S. Sankar, A. Karmakar, R. Madhu, K. Bera and S. Kundu, *Sustainable Energy Fuels*, 2021, **5**, 6215–6268.
15 X. Xie, L. Du, L. Yan, S. Park, Y. Qiu, J. Sokolowski, W. Wang and Y. Shao, *Adv. Funct. Mater.*, 2022, **32**, 2110036.
16 L. Han, S. Dong and E. Wang, *Adv. Mater.*, 2016, **28**, 9266–9291.
17 J. Ni, Z. Shi, Y. Wang, J. Yang, H. Wu, P. Wang, M. Xiao, C. Liu and W. Xing, *eScience*, 2025, **5**, 100295.
18 Q. Wang, Y. Cheng, H. B. Tao, Y. Liu, X. Ma, D. S. Li, H. B. Yang and B. Liu, *Angew. Chem.*, 2023, **135**, e202216645.
19 F.-Y. Chen, Z.-Y. Wu, Z. Adler and H. Wang, *Joule*, 2021, **5**, 1704–1731.
20 H. Wan, F. Chen, W. Ma, X. Liu and R. Ma, *Nanoscale*, 2020, **12**, 21479–21496.
21 Y. Xia, H. Cheng, H. He and W. Wei, *Commun. Eng.*, 2023, **2**, 22.
22 M. S. Burke, S. Zou, L. J. Enman, J. E. Kellon, C. A. Gabor, E. Pledger and S. W. Boettcher, *J. Phys. Chem. Lett.*, 2015, **6**, 3737–3742.
23 F. Dionigi, Z. Zeng, I. Sinev, T. Merzdorf, S. Deshpande, M. B. Lopez, S. Kunze, I. Zegkinoglou, H. Sarodnik and D. Fan, *Nat. Commun.*, 2020, **11**, 2522.
24 M. S. Burke, L. J. Enman, A. S. Batchellor, S. Zou and S. W. Boettcher, *Chem. Mater.*, 2015, **27**, 7549–7558.
25 F. Dionigi and P. Strasser, *Adv. Energy Mater.*, 2016, **6**, 1600621.
26 S. Klaus, Y. Cai, M. W. Louie, L. Trotochaud and A. T. Bell, *J. Phys. Chem. C*, 2015, **119**, 7243–7254.
27 Y. Ou, L. P. Twight, B. Samanta, L. Liu, S. Biswas, J. L. Fehrs, N. A. Sagui, J. Villalobos, J. Morales-Santelices and D. Antipin, *Nat. Commun.*, 2023, **14**, 7688.
28 L. Trotochaud, S. L. Young, J. K. Ranney and S. W. Boettcher, *J. Am. Chem. Soc.*, 2014, **136**, 6744–6753.
29 F. Dionigi, Z. Zeng, I. Sinev, T. Merzdorf, S. Deshpande, M. B. Lopez, S. Kunze, I. Zegkinoglou, H. Sarodnik, D. Fan, A. Bergmann, J. Drnec, J. F. d. Araujo, M. Gliech, D. Teschner, J. Zhu, W.-X. Li, J. Greeley, B. R. Cuenya and P. Strasser, *Nat. Commun.*, 2020, **11**, 2522.
30 F. Dionigi, J. Zhu, Z. Zeng, T. Merzdorf, H. Sarodnik, M. Gliech, L. Pan, W. X. Li, J. Greeley and P. Strasser, *Angew. Chem.*, 2021, **133**, 14567–14578.
31 C. S. Lim, C. K. Chua, Z. Sofer, K. Klímová, C. Boothroyd and M. Pumera, *J. Mater. Chem. A*, 2015, **3**, 11920–11929.
32 Z. Yan, H. Liu, Z. Hao, M. Yu, X. Chen and J. Chen, *Chem. Sci.*, 2020, **11**, 10614–10625.
33 Z. Yan, H. Sun, X. Chen, H. Liu, Y. Zhao, H. Li, W. Xie, F. Cheng and J. Chen, *Nat. Commun.*, 2018, **9**, 2373.
34 C. C. L. McCrory, S. Jung, J. C. Peters and T. F. Jaramillo, *J. Am. Chem. Soc.*, 2013, **135**, 16977–16987.
35 D. Tench and L. F. Warren, *J. Electrochem. Soc.*, 1983, **130**, 869.
36 J. Reyes-Morales and J. E. Dick, *Acc. Chem. Res.*, 2023, **56**, 1178–1189.
37 M. W. Glasscott, A. D. Pendergast and J. E. Dick, *ACS Appl. Nanomater.*, 2018, **1**(10), 5702–5711.
38 M. W. Glasscott, A. D. Pendergast, S. Goines, A. R. Bishop, A. T. Hoang, C. Renault and J. E. Dick, *Nat. Commun.*, 2019, **10**, 2650.
39 Y. E. Jeun, J. H. Park, J. Y. Kim and H. S. Ahn, *Chem.–Eur. J.*, 2020, **26**, 4039–4043.
40 S. Paul, J. F. Koons, M. L. Harrigan, K. Roy and J. E. Dick, *Electroanalysis*, 2025, **37**, e12043.
41 J. F. Koons, S. Paul and J. E. Dick, *Langmuir*, 2025, 5524–5533.
42 A. J. Bard, L. R. Faulkner and H. S. White, *Electrochemical Methods: Fundamentals and Applications*, John Wiley & Sons, 2022.

43 M. C. Biesinger, B. P. Payne, A. P. Grosvenor, L. W. M. Lau, A. R. Gerson and R. S. C. Smart, *Appl. Surf. Sci.*, 2011, **257**, 2717–2730.
44 N. Fairley, V. Fernandez, M. Richard-Plouet, C. Guillot-Deudon, J. Walton, E. Smith, D. Flahaut, M. Greiner, M. Biesinger and S. Tougaard, *Appl. Surf. Sci. Adv.*, 2021, **5**, 100112.
45 Y. Li and C. Zhao, *ACS Catal.*, 2017, **7**, 2535–2541.
46 T. B. Clarke and J. E. Dick, *J. Phys. Chem. Lett.*, 2022, **13**, 3338–3341.
47 Z. Zeng, M. K. Y. Chan, Z.-J. Zhao, J. Kubal, D. Fan and J. Greeley, *J. Phys. Chem. C*, 2015, **119**, 18177–18187.
48 B. Beverskog and I. Puigdomenech, *Corros. Sci.*, 1997, **39**, 107–114.
49 J. K. Lee, D. Samanta, H. G. Nam and R. N. Zare, *Nat. Commun.*, 2018, **9**, 1562.
50 S. Zhong, P. Cui, Y. Yan, H. Wei, L. Du, Q. Chen and W. Sun, *Langmuir*, 2025, 9019–9026.
51 X. Chen, Y. Xia, Y. Wu, Y. Xu, X. Jia, R. N. Zare and F. Wang, *J. Am. Chem. Soc.*, 2024, **146**, 10868–10874.
52 H. Wei, E. P. Vejerano, W. Leng, Q. Huang, M. R. Willner, L. C. Marr and P. J. Vikesland, *Proc. Natl. Acad. Sci. U. S. A.*, 2018, **115**, 7272–7277.
53 L. E. Krushinski and J. E. Dick, *Proc. Natl. Acad. Sci. U. S. A.*, 2024, **121**, e2321064121.
54 L. E. Krushinski, P. J. Herchenbach and J. E. Dick, *Proc. Natl. Acad. Sci. U. S. A.*, 2024, **121**, e2416353121.